PNAS
www.pnas.org

Supplementary Information for

Mapping Hydroxyl Variability throughout the Global Remote Troposphere via Synthesis of Airborne and Satellite Formaldehyde Observations

Glenn M. Wolfe*, Julie M. Nicely, Jason M. St. Clair, Thomas F. Hanisco, Jin Liao, Luke D. Oman, William B. Brune, David Miller, Alexander Thames, Gonzalo González Abad, Thomas B. Ryerson, Chelsea R. Thompson, Jeff Peischl, Kathryn McCain, Colm Sweeney, Paul O. Wennberg, Michelle Kim, John D. Crounse, Samuel R. Hall, Kirk Ullmann, Glenn Diskin, Paul Bui, Cecilia Chang, Jonathan Dean-Day

*Correspondence to glenn.m.wolfe@nasa.gov

Contents

www.pnas.org/cgi/doi/10.1073/pnas.1821661116

Text S1. Derivation of Column-Integrated Steady State Relationship

Here we show the derivation of Eqn. (3) from Eqn. (2) (both appearing in the main text). Equation (2) presents the instantaneous in situ steady state relationship between HCHO and OH:

$$[HCHO] = \frac{\alpha k'_{OH}[OH] + P_0}{j_{HCHO} + k_{HCHO+OH}[OH]} \quad (2)$$

Here, α is the effective HCHO yield weighted over all OH reactions (unitless), k'_{OH} is the pseudo-first order OH reactivity (s^{-1}), P_O represents HCHO production from minor non-OH HCHO sources ($cm^{-3}\ s^{-1}$), j_{HCHO} is the HCHO photolysis frequency (s^{-1}, both channels), and $k_{HCHO+OH}$ is the rate coefficient for reaction of HCHO with OH ($cm^3\ s^{-1}$). Moving the denominator to the left and integrating over altitude gives

$$\int_0^z (j_{HCHO} + k_{HCHO+OH}[OH])[HCHO]dz = \int_0^z \alpha k'_{OH}[OH]dz + \int_0^z P_0 dz \quad (S1)$$

Next, we define the following column-integrated quantities.

$$k'_{HCHO} = \frac{\int_0^z (j_{HCHO} + k_{HCHO+OH}[OH])[HCHO]dz}{\int_0^z [HCHO]dz} \quad (S2)$$

$$s_{OH} = \frac{\int_0^z \alpha k'_{OH}[OH]dz}{\int_0^z [OH]dz} \quad (S3)$$

The HCHO reactivity, k'_{HCHO}, is the integrated HCHO loss frequency weighted by HCHO abundance and is calculated explicitly from observations for each profile as described in Methods. The slope parameter, s_{OH}, is the integrated HCHO production rate (from OH reactions only) normalized by OH abundance (or, equivalently, the HCHO production frequency weighted by OH abundance). The latter is treated as a constant and calculated via a fit of ATom data. Substitution of (S2) and (S3) into (S1) gives

$$k'_{HCHO} \int_0^z [HCHO]dz = s_{OH} \int_0^z [OH]dz + \int_0^z P_0 dz \quad (S4)$$

Finally, replacing integrals by the prefix Ω and moving k'_{HCHO} gives Eqn. (3) from the main text:

$$\Omega[HCHO] = s_{OH} \frac{\Omega[OH]}{k'_{HCHO}} + \Omega[HCHO]_0 \quad (3)$$

Here the HCHO column attributable to non-OH sources, $\Omega[HCHO]_0 = \Omega P_0 / k'_{HCHO}$, is the intercept in the fit to ATom data.

Equation (3) is only pseudo-linear with respect to OH, as the k'_{HCHO} term includes a contribution from OH. As discussed in Sect. 3.1 of the main text, this assumption is consistent with the fact that photolysis generally dominates the HCHO loss budget.

Text S2. OMI Evaluation

HCHO vertical column densities are derived from measurements taken by the Ozone Monitoring Instrument (OMI) flying on NASA's Aura satellite (1). Aura follows a sun-synchronous orbit with an equatorial overpass time of 13:30 LST. OMI measures spectrally-resolved solar back-scattered radiation in the UV/Visible range with a nominal pixel size of 13 x 24 km^2 at nadir and global coverage every ~2 days. HCHO slant column densities are retrieved by spectrally fitting HCHO absorption in the UV. Vertical column densities are derived from slant columns using corrections to account for radiation scatter, instrument sensitivity, background offsets, and other issues.

Retrieval of total column formaldehyde (Ω[HCHO]) from space-based remote sensors is a complex, multi-step process requiring numerous model inputs and various assumptions. As outlined in the main text, the general agreement of OMI and ATom observations gives us confidence that the OMI-SAO v003 product captures the main features of Ω[HCHO] variability in remote regions. Here we examine two aspects of the retrieval in closer detail: a priori vertical profiles and the reference sector offset correction.

A priori HCHO vertical profiles are one component of the air mass factors (AMF) used to convert slant column densities to vertical column densities. The a priori enters the AMF calculation as a "shape factor," which is the vertical profile normalized by the total column density. Errors in the shape factor can degrade retrieval accuracy, as the sensitivity of solar scattering-based instruments is inherently altitude-dependent (2). A prioris are typically derived from a global model; the OMI-SAO v003 retrieval uses a monthly GEOS-Chem climatology at 2° x 2.5° (3). On average, the OMI-SAO a priori is ~18% lower than the mean HCHO profile for ATom 1 and 2 (Fig. S5a), consistent with previous model-measurement comparisons in remote regions (4, 5). Despite the underestimate of absolute magnitude, the shape of both profiles is quite similar. Area normalization and multiplication by the average scattering weight profile yields an AMF density function (Fig. S5b), which is the integrand for AMF calculation. AMF density functions are similar for OMI and ATom. Roughly 10% of the OMI AMF density resides above 10 km. To calculate the "full" AMF for ATom, we integrate the ATom AMF density from 0 – 10 km and add the difference between OMI AMFs calculated from 0 – 10 km and over the full domain (0 – 36 km). ATom AMFs calculated in this fashion are higher than OMI by 4 ± 7% (Fig. S5c). Thus, model a prioris do not introduce significant error into OMI Ω[HCHO] over the ATom study region.

"Reference sector" normalization corrects for detector drift and, at high latitudes, spectral contamination by BrO (3, 6). Essentially, the correction involves selecting a region in the remote Pacific (currently 140°W – 160°W for OMI-SAO), averaging slant columns into latitudinal bands, subtracting these values from all slant columns within each band, and adding back in latitude- and month-dependent GEOS-Chem climatological columns from the reference sector region. Thus, some fraction of the retrieval product is effectively a model-simulated value. Figure S6 illustrates the absolute and fractional change in Ω[HCHO] resulting from this correction. The correction is typically within ±30% of Ω[HCHO] within the Tropics but can exceed -100% at higher latitudes, especially in the wintertime hemispheres. Even in regions where the correction is relatively large, however, OMI Ω[HCHO] exhibits significant spatial variability that is consistent with ATom observations (Fig. 1). Note, for example, the significant difference in Ω[HCHO] for

ATom 2 between the Northern Hemisphere Pacific and Atlantic basins. Figure S7 compares ATom observations to the OMI-SAO Ω[HCHO] retrievals prior to application of this correction. Not surprisingly, all correlation metrics are degraded relative to the corrected product shown in Fig. 3 of the main text. Even so, the correlation between OMI and ATom is still moderate (r^2 = 0.39) and there remains a clear linear relationship. Thus, we contend that the OMI-SAO retrieval contains real information about the atmosphere even prior to applying the reference sector correction.

Text S3. GMI Simulation and Evaluation

The MERRA-2 GMI simulation couples the Goddard Earth Observing System version 5 (GEOS-5) general circulation model (7) to the comprehensive Global Modeling Initiative (GMI) stratosphere-troposphere chemical mechanism (8-10). The GMI chemical mechanism includes 117 species, 322 chemical reactions, and 81 photolysis reactions. The SMVGEAR II algorithm (11) is used to integrate the chemical mass balance equations. The mechanism includes a detailed description of O_3-NO_x-hydrocarbon chemistry, and rate coefficients have been updated to the latest JPL recommendations (12) where possible. Photolysis rates are determined with an updated version of Fast-JX (13). The GMI mechanism includes the impact of solar cycle variability on the actinic flux (9). The concentrations of methane, other greenhouse gases, and ozone depleting substances are specified as a surface boundary condition based on observed values. Fossil fuel and biofuel emissions of trace gases come from the MACCity inventory (14), scaled up through present using the Representative Concentration Pathways (RCP 8.5) emissions. Daily biomass burning emissions are from the GFEDv4.1s dataset (15), which includes emissions from small fires (16).

Under the GEOS-5 framework, the GMI chemical mechanism can be coupled to several different circulation models. The MERRA-2 GMI simulation uses the GEOS-5 model in Replay mode at 0.5° horizontal resolution on the cubed sphere with outputs that have the same 0.625° x 0.5° grid as the MERRA-2 Reanalysis and was run from 1980-2017. A subset was rerun over the ATom1 and 2 time periods saving high temporal resolution (1 hourly) output for the analysis done in this study.

GMI output is used to estimate the sampling variance for individual ATom profiles for comparison with OMI as discussed in Sect. 3.2 of the main text. By "sampling variance," we mean the uncertainty associated with acquiring a single hourly sample from a month-long distribution. First, the standard deviation of Ω[HCHO] for each grid box is calculated using all hourly output over each campaign. Next, these values are sampled along the ATom flight path by averaging all grid boxes traversed by a given profile (analogous to how OMI retrievals are sampled), yielding a model-derived sampling standard deviation for each profile. Average standard deviations are uncorrelated with modeled or measured Ω[HCHO], thus we take their mean (0.45×10^{15} cm^{-2}) as a reasonable estimate of sampling-induced uncertainty across the ATom dataset.

Figure S9 shows the model relationship between Ω[HCHO] and $\Omega[OH]/k'_{HCHO}$, in analogy with Fig. 2(a) in the main text. For this plot, model output is filtered to only include non-land areas and SZA < 80°. More than 99% of model columns fall within the range sampled by ATom. The full distribution of model output is much broader, with occasional high Ω[HCHO] related to non-methane hydrocarbon influence (typically near coastal regions). Model output is loosely consistent with ATom observations but is offset toward lower Ω[HCHO] or higher $\Omega[OH]/k'_{HCHO}$. This may be related to one or more potential model issues (over-estimated HCHO deposition, model OH fields, etc.), and is consistent with the findings of other studies (4, 5). We show this plot mainly to illustrate the qualitative agreement of ATom observations and GMI output.

Model output is needed to constrain global HCHO loss frequencies, creating the potential for model-induced bias in inferred Ω[OH]. Of particular concern is the model OH distribution, as a non-

negligible fraction of HCHO loss occurs via reaction with OH. Thus, errors in model OH fields could propagate into k'_{HCHO}. GMI j'_{HCHO} and k'_{HCHO} follow the same general relationship as ATom (Fig. S10), but the model also shows a somewhat different distribution of j'_{HCHO}/k'_{HCHO} ratios. Some differences may be due to more OH in certain air masses not sampled by ATom (e.g. coastal outflow with elevated NO_x), but as mentioned above these are a minor fraction of total output. Other potential explanations include cloud-related bias in model J-values (17) or bias in model OH or temperature fields. A full model evaluation is outside the scope of the present work. Even in the most extreme GMI cases, photolysis is always 50% or more of total HCHO loss.

To curtail the above issue, we use the ATom relationship between total (k'_{HCHO}) and photolysis (j'_{HCHO}) loss frequencies to rescale GMI j'_{HCHO}. This correlation is strong (r^2 = 0.94, Fig. S11), and use of predicted k'_{HCHO} in Eqn. (4) does not significantly alter ATom fit coefficients (Fig. S12). Column-weighted GMI j'_{HCHO} is calculated using the analogue of Eqn. (S2) and integrating from the ground to the model tropopause. Daily j'_{HCHO} values are averaged over each mission and transformed into k'_{HCHO} using the quadratic scaling factors shown in Fig. S11a. Figure S13 shows GMI fields for mission-average j'_{HCHO} and scaled k'_{HCHO}; spatial patterns in both are consistent with ATom observations. Additional potential sources of bias in GMI-derived HCHO loss frequencies include model cloud cover and HCHO vertical profiles; below we examine each using ATom observations.

Model cloud cover could bias campaign-average j'_{HCHO} if it is statistically different from the real atmosphere. Clouds enhance or reduce photolysis, but their aggregate effects are highly location- and model-dependent (17). Figure S14b shows fair agreement for j'_{HCHO} between ATom and GMI in terms of both magnitude and variability. This provides some confidence in the GMI product and suggests that we do not need to filter model output for cloud cover. The latter point is also supported by the fact that GMI j'_{HCHO} is relatively insensitive to clouds for all but the clearest conditions, where column-average j'_{HCHO} is reduced by 10 – 15% (Fig. S14a). This result is somewhat surprising given the dramatic difference in albedo between the ocean surface and clouds, but this may indicate partial compensation of enhancements and reductions when averaging over the column and over multiple days.

Another potential concern is the weighting of j'_{HCHO} by the model's HCHO vertical profile. To assess the importance of the HCHO profile shape, we perform a sensitivity test using ATom observations where j'_{HCHO} is re-calculated for each profile using the mean vertical HCHO distribution over all of ATom 1 and 2. Profiles vary substantially over the mission, but the magnitude and shape of the vertical profile has a generally negligible impact on j'_{HCHO} (Fig. S15). This result also supports the use of differing altitude limits for the various calculation inputs (GMI j'_{HCHO} is integrated from the ground to the model tropopause).

Text S4. Potential Influence of Clear-sky Bias on X[OH]

Both airborne and satellite observations are inherently biased toward conditions with low cloud cover. ATom profiles typically occurred in partly cloudy or clear conditions and tended to avoid heavily overcast or stormy areas. OMI observations are filtered at the single-pixel level for cloud cover < 30% to ensure retrieval quality. Clouds cover 70 – 80% of the ocean on average (18), thus the questions arises: is the X[OH] product derived here representative of the whole atmosphere, or is there a bias relative to "all sky" OH? To unravel the complex effects of clouds, we consider separately the cloud influence on each of the three major terms in Eqn. (4) of the main text: the slope, s_{OH}; the HCHO column, Ω[HCHO]; and the HCHO loss frequency, k'_{HCHO}.

The slope parameter, s_{OH}, reflects the column-integrated steady state relationship between HCHO production/loss and OH abundance. We first consider this from the HCHO production perspective. Following Eqn. (S3), variability in s_{OH} is a function of the effective HCHO yield, α, and total OH reactivity, k'_{OH} (weighted by OH abundance). Both are a function of chemical composition. CO and CH_4 are the dominant components of k'_{OH} in the remote atmosphere, with reactive hydrocarbons occasionally making important regional contributions. We do not expect cloud cover to induce significant variability in k'_{OH}. The effective HCHO yield depends on the speciation of OH sinks and the balance of RO_2 fates (mainly loss via NO and HO_2). Clouds impart similar perturbations to $J(NO_2)$ and $J(O^1D)$ on average (17), thus we also do not expect a large clear-sky bias in this term. Indeed we expect α to vary little in the remote atmosphere, as all CH_4 oxidation pathways eventually lead to HCHO. As noted in Sect. 3.1 of the main text, s_{OH} is also sensitive to the OH vertical profile. Clouds can enhance OH in the middle/upper troposphere, and in such cases the ATom-derived value of s_{OH} is expected to be higher than the "true" column-specific value. If we were applying the pseudo-linear transform to "all sky" HCHO columns, this could impart a low bias of ~30% to inferred X[OH] in regions with heavy cloud cover in the lower/middle troposphere (Fig. S4a, see points above observed $\Omega[OH] = 6 \times 10^{12}$ cm^{-2}). Since OMI retrievals are cloud-filtered, however, the ATom-derived value of s_{OH} is an appropriate estimate. Based on the above arguments, we do not expect a cloud-related bias in X[OH] due to s_{OH}.

Alternatively, we can consider variations in s_{OH} from the HCHO loss perspective. From Eqn. (3), the slope is proportional to the ratio $k'_{HCHO}\Omega[HCHO]:\Omega[OH]$. Both terms scale with UV radiation; indeed, this is the main mode of variability driving the correlation in Fig. 2. Thus, in general we expect radiative cloud effects to mostly compensate one another for large-scale changes in cloud cover (e.g. clear-sky vs solid overcast). Mixed cloud cover is a more complex situation, as this can lead to intermittent high or low OH where HCHO is not in instantaneous steady state (the HCHO loss frequency responds rapidly, but the HCHO abundance has a time constant of hours). In such cases, HCHO is still representative of the oxidative capacity averaged over its lifetime of several hours. Furthermore, integration over the full atmospheric column tends to smooth out localized perturbations. Again, we do not expect cloud cover to significantly alter s_{OH}, and thus we do not suspect a bias in this parameter as derived from ATom observations.

If OMI Ω[HCHO] retrievals (which are cloud-filtered) differ systematically from all-sky Ω[HCHO], then OMI observations could impart a bias to X[OH]. We cannot easily test such effects with available observations, so we use GMI output to estimate the influence of cloud filtering on retrieval

representativeness. For this sensitivity test, we average hourly GMI output over each mission using either all columns ("all sky") or only columns with a cloud fraction of 0.3 or less ("clear sky"). Figure S16 shows that the clear sky bias is small (< ±5%) throughout the tropics and subtropics. Larger deviations, up to ±50%, can occur in regions with low insolation and/or persistent cloud cover, notably the Southern Ocean and the NH mid-latitudes in February. The strongest biases are mostly negative, indicating that persistent cloud cover tends to *increase* total column HCHO in GMI. Such effects also depend on cloud top pressure, with lower clouds leading to enhanced photochemistry in a larger fraction of the column. The normalized mean bias in clear sky Ω[HCHO] is -4.8% for all non-land areas, and this decreases to -0.03% when weighting by tropospheric mass (as is done when spatially averaging X[OH]). Thus, OMI Ω[HCHO] cloud filtering likely does not impart a bias to large-scale averages of X[OH] but may impact some mid-latitude and polar regions where HCHO and OH are typically near the OMI precision estimate of 1×10^{15} cm^{-2}.

The effects of cloud cover on column-average HCHO photolysis, j'_{HCHO}, are discussed in Text S3. We find that GMI j'_{HCHO} is relatively insensitive to clouds and, more importantly, that the variability and magnitude of GMI j'_{HCHO} is consistent with ATom observations (Fig. S14). The link between j'_{HCHO} and k'_{HCHO} (which includes OH loss) is well-described by the quadratic ATom relationship (Fig. S11). The curvature of this correlation is driven by the stronger UV dependence of $J(O^1D)$ relative to J(HCHO), and we do not expect clouds to cause a significant deviation from the observed relationship.

In summary, we find little evidence that X[OH] will contain biases due to preferential clear-sky sampling in ATom or OMI observations. This finding is consistent with the agreement between X[OH] and MCF-based global inferences of OH abundance and the NH/SH ratio as described in the main text. Based on GMI output, biases in Ω[HCHO] of up to -50% are possible in the Southern Ocean. Columns in this region are typically quite low (< 1×10^{15} cm^{-2}, Fig. 1), but this bias may partially explain the discrepancy between X[OH] and the box model estimates of Spivakovsky*, et al.* (19) for ATom 2 (Fig. S18). It may be possible to correct for such biases using satellite-based cloud products. Ideally, such a correction would be tied to in situ observations that provide sufficient statistics on how clouds influence tropospheric column composition and chemistry.

Text S5. Global OH Burden Reconciliation

Here we explore the potential utility of combining X[OH] with a top-down global constraint on oxidizing capacity. The bi-seasonal average of remote or "ocean" X[OH] covers ~72% of global tropospheric mass and, given the agreement between ATom 1 and 2, likely approximates an annual average. Roughly 27% of tropospheric mass resides over land in this scenario, while the remaining < 1% is near the poles where OH is negligibly small. Thus, merging these observations with an MCF-based global estimate may elucidate the variability of terrestrial OH. It is not immediately obvious whether OH should be higher or lower over land, as this region contains both elevated sources (NO_x stimulating radical turnover) and sinks (short-lived non-methane hydrocarbons).

Recent studies have quantified total oxidizing capacity in terms of CH_4 lifetime (τ_{CH4}), and we will adopt the same perspective here. For the global methane lifetime, we use the Prather et al. (20) estimate of 11.2 ± 1.3 y for the global CH_4 lifetime. Though this value is derived for the year 2010, inter-annual variability in OH is expected to be small (2.3 ± 1.5%) (21) compared to the 1σ uncertainty. Next, we define 3 regions: "water," comprising all non-land areas with valid OMI observations; "land," comprising all remaining areas with valid OMI observations; and "poles," where OMI observations are not valid. The global CH_4 loss rate is the sum of loss rates over the individual regions:

$$\frac{M_{Globe}}{\tau_{Globe}} = \frac{M_{Ocean}}{\tau_{Ocean}} + \frac{M_{Land}}{\tau_{Land}} + \frac{M_{Poles}}{\tau_{Poles}} \quad \text{(S5)}$$

Here, *M* refers to the mass of CH_4 over a given region as determined from GMI output (Table S4). The "poles" lifetime is assumed infinite (negligibly small OH).

The "ocean" CH_4 lifetime is calculated from X[OH] as

$$\tau_{Ocean} = \frac{\sum_i M_i}{\sum_i M_i k(T_i) X[OH]_i} \quad \text{(S6)}$$

M_i is the mass of CH_4 in each column, T_i is the mass-weighted column-average air temperature, and $k(T_i)$ is the rate coefficient for CH_4 + OH from the most recent JPL recommendation (12). For the bi-seasonal average, this yields an "ocean" CH_4 lifetime of 11.4 ± 3.7 y (Table S4). Technically, the temperature used in this calculation should be weighted by the rate of CH_4 mass loss via OH to properly account for co-location of OH and CH_4. Doing so requires relying on 3-D GMI OH fields, and we find that this leads to a significantly shorter lifetime of ~8.2 y. The correlation between global average OH and CH_4 lifetime follows a well-defined relationship (Fig. S19), and our results concur best with this trend when using mass-weighted air temperature.

Via mass balance (Eqn. (S5)), we thus arrive at a "land" CH_4 lifetime of 9.8 ± 5.4 y. We account here for partial error correlation of the global and "ocean" lifetimes due to rate coefficient uncertainty. As we are effectively taking the difference of two large numbers, however, the uncertainty in the "land" lifetime is relatively large.

Given the substantial uncertainties, it is not possible to draw definitive conclusions regarding the nature of land/water contrast in oxidizing capacity. Our best estimate indicates that OH is ~14% higher

over land on an annual average, but we cannot state this with confidence. We can repeat this calculation for individual missions, scaling the global CH_4 lifetime using a typical model annual cycle (22) (Table S4). It is similarly difficult to discern seasonality, and the derived "land" lifetimes are very sensitive to the monthly lifetime scaling factor. More work is needed to understand how to synthesize bottom-up and top-down OH estimates.

Text S6. Box Model Simulation

Box model results are used primarily to illustrate the average source and sink distributions of OH and HCHO and to estimate a minor correction to measurement-constrained OH production rates. These results are not central to our analysis, thus we only provide here a brief summary of the simulation setup. Further details on measurement methods and uncertainties of observations used in the box model analysis are available on the ATom data archive.

Measurement-constrained box model calculations were carried out using the Framework for 0-D Atmospheric Modeling (F0AM v3.2, available at https://github.com/AirChem/F0AM/) (23). Constraints are taken from the ATom "Modeling Data Stream," which is a 10-second merge of in situ observations with linear interpolation to fill missing observations (further details can be found at https://espoarchive.nasa.gov/archive/browse/atom/DC8/MDS). This merge is designed to evaluate photochemical reactivity (24) and is adequate for our application. For model input, we further average observations from 10 to 60 seconds. Meteorological constraints include ambient temperature and pressure, water vapor, and photolysis frequencies for 15 compounds. Solar zenith angles are calculated from aircraft location and time. Chemical constraints include CH_4, CO, O_3, PAN, HNO_3, HO_2NO_2, H_2O_2, methyl and ethyl nitrate, alkanes (ethane, propane, i-butane, n-butane), alkenes (ethene, isoprene), ethyne, aromatics (benzene, toluene, xylenes), and oxygenated hydrocarbons (formaldehyde, acetaldehyde, methyl hydrogen peroxide, and acetone). NO_x concentrations are constrained using a fixed NO_2 concentration for each set of observations, iteratively adjusted such that model-predicted NO matches observed NO. Chemistry is based on the Master Chemical Mechanism v3.3.1 (25) with several additional reactions: photolysis of HO_2NO_2, reaction of CH_4 with $O(^1D)$, and reaction of CH_3O_2 with OH (26, 27). For each set of constraints, the model is run forward in time for three days to reach steady state. All constraints except photolysis frequencies are held constant during integration, and the photolysis frequency update time is 30 minutes.

Text S7. Regarding North/South Hemisphere OH Ratios

Our calculation of the NH/SH ratio uses the geographic equator for separation, though some studies advocate the intertropical convergence zone (ITCZ) as a more natural mixing boundary (28). It is difficult to quantify the expected differences between these two options with the current dataset, as the ITCZ location varies with location and time. MCF inversion studies report a typical decrease of 7 – 12% in the multiannual NH/SH ratio when using the ITCZ as the delineator (28, 29), and we expect a similar effect on the bi-seasonal average reported in Table 1 of the main text. The ITCZ is situated significantly farther north of the equator during the Boreal summer than it is south during the Austral summer. Thus, we expect a significant decrease in the NH/SH ratio for ATom 1 and a slight increase in the ratio for ATom 2 when using the ITCZ for delineation.

SI References

1. Levelt PF*, et al.* (2006) The Ozone Monitoring Instrument. *Ieee Transactions on Geoscience and Remote Sensing* 44(5):1093-1101.
2. Zhu L*, et al.* (2016) Observing atmospheric formaldehyde (HCHO) from space: validation and intercomparison of six retrievals from four satellites (OMI, GOME2A, GOME2B, OMPS) with SEAC4RS aircraft observations over the southeast US. *Atmos. Chem. Phys.* 16(21):13477-13490.
3. González Abad G*, et al.* (2015) Updated Smithsonian Astrophysical Observatory Ozone Monitoring Instrument (SAO OMI) formaldehyde retrieval. *Atmos. Meas. Tech.* 8:19-32.
4. Anderson DC*, et al.* (2017) Formaldehyde in the Tropical Western Pacific: Chemical sources and sinks, convective transport, and representation in CAM-Chem and the CCMI models. *J. Geophys. Res. Atmos.*:n/a-n/a.
5. Nicely JM*, et al.* (2016) An observationally constrained evaluation of the oxidative capacity in the tropical western Pacific troposphere. *J. Geophys. Res. Atmos.*
6. Khokhar MF*, et al.* (2005) Satellite observations of atmospheric SO2 from volcanic eruptions during the time-period of 1996-2002. *Atmospheric Remote Sensing: Earth's Surface, Troposphere, Stratosphere and Mesosphere - I,* Advances in Space Research-Series, eds Burrows JP & Eichmann KU), Vol 36, pp 879-887.
7. Molod A, Takacs L, Suarez M, & Bacmeister J (2015) Development of the GEOS-5 atmospheric general circulation model: evolution from MERRA to MERRA2. *Geosci. Mod. Dev.* 8(5):1339-1356.
8. Duncan BN, Strahan SE, Yoshida Y, Steenrod SD, & Livesey N (2007) Model study of the cross-tropopause transport of biomass burning pollution. *Atmos. Chem. Phys.* 7(14):3713-3736.
9. Nielsen JE*, et al.* (2017) Chemical Mechanisms and Their Applications in the Goddard Earth Observing System (GEOS) Earth System Model. *Journal of Advances in Modeling Earth Systems* 9(8):3019-3044.
10. Oman LD*, et al.* (2013) The ozone response to ENSO in Aura satellite measurements and a chemistry-climate simulation. *J. Geophys. Res. Atmos.* 118(2):965-976.
11. Jacobson MZ (1995) COMPUTATION OF GLOBAL PHOTOCHEMISTRY WITH SMVGEAR-II. *Atmos. Env.* 29(18):2541-2546.
12. Burkholder JB*, et al.* (2015) Chemical Kinetics and Photochemical Data for Use in Atmospheric Studies, Evaluation No. 18, JPL Publication 15-10, Jet Propulsion Laboratory, Pasadena, CA, http://jpldataeval.jpl.nasa.gov.
13. Bian HS & Prather MJ (2002) Fast-J2: Accurate simulation of stratospheric photolysis in global chemical models. *J. Atmos. Chem.* 41(3):281-296.
14. Granier C*, et al.* (2011) Evolution of anthropogenic and biomass burning emissions of air pollutants at global and regional scales during the 1980-2010 period. *Climatic Change* 109(1-2):163-190.
15. Giglio L, Randerson JT, & van der Werf GR (2013) Analysis of daily, monthly, and annual burned area using the fourth-generation global fire emissions database (GFED4). *Journal of Geophysical Research-Biogeosciences* 118(1):317-328.
16. Randerson JT, Chen Y, van der Werf GR, Rogers BM, & Morton DC (2012) Global burned area and biomass burning emissions from small fires. *Journal of Geophysical Research-Biogeosciences* 117.
17. Hall SR*, et al.* (2018) Cloud impacts on photochemistry: building a climatology of photolysis rates from the Atmospheric Tomography mission. *Atmos. Chem. Phys.* 18(22):16809-16828.
18. Stubenrauch CJ*, et al.* (2013) Assessment of Global Cloud Datasets from Satellites: Project and Database Initiated by the GEWEX Radiation Panel. *Bull. Am. Met. Soc.* 94(7):1031-1049.

19. Spivakovsky CM*, et al.* (2000) Three-dimensional climatological distribution of tropospheric OH: Update and evaluation. *J. Geophys. Res. Atmos.* 105(D7):8931-8980.
20. Prather MJ, Holmes CD, & Hsu J (2012) Reactive greenhouse gas scenarios: Systematic exploration of uncertainties and the role of atmospheric chemistry. *Geophys. Res. Lett.* 39.
21. Montzka SA*, et al.* (2011) Small Interannual Variability of Global Atmospheric Hydroxyl. *Science* 331(6013):67-69.
22. Nicely JM*, et al.* (2017) Quantifying the causes of differences in tropospheric OH within global models. *J. Geophys. Res. Atmos.* 122(3):1983-2007.
23. Wolfe GM, Marvin MM, Roberts SJ, Travis KR, & Liao J (2016) The Framework for 0-D Atmospheric Modeling (F0AM) v3.1. *Geosci. Model Dev.* 9:3309-3319.
24. Prather MJ*, et al.* (2018) How well can global chemistry models calculate the reactivity of short-lived greenhouse gases in the remote troposphere, knowing the chemical composition. *Atmos. Meas. Tech.* 11(5):2653-2668.
25. Jenkin ME, Young JC, & Rickard AR (2015) The MCM v3.3.1 degradation scheme for isoprene. *Atmos. Chem. Phys.* 15:11433-11459.
26. Assaf E*, et al.* (2017) The Reaction between CH3O2 and OH Radicals: Product Yields and Atmospheric Implications. *Env. Sci. Technol.* 51(4):2170-2177.
27. Assaf E, Song B, Tomas A, Schoemaecker C, & Fittschen C (2016) Rate Constant of the Reaction between CH3O2 Radicals and OH Radicals Revisited. *J. Phys. Chem. A* 120(45):8923-8932.
28. Montzka SA*, et al.* (2000) New observational constraints for atmospheric hydroxyl on global and hemispheric scales. *Science* 288(5465):500-503.
29. Patra PK*, et al.* (2014) Observational evidence for interhemispheric hydroxyl-radical parity. *Nature* 513(7517):219-223.
30. Cazorla M*, et al.* (2015) A new airborne laser-induced fluorescence instrument for in situ detection of Formaldehyde throughout the troposphere and lower stratosphere. *Atmos. Meas. Tech.* 8:541-552.
31. Faloona IC*, et al.* (2004) A laser-induced fluorescence instrument for detecting tropospheric OH and HO2: Characteristics and calibration. *J. Atmos. Chem.* 47:139-167.
32. Ryerson T*, et al.* (1999) Design and initial characterization of an inlet for gas-phase NOy measurements from aircraft. *J. Geophys. Res. Atmos.* 104(D5):5483-5492.
33. Ryerson T, Williams E, & Fehsenfeld F (2000) An efficient photolysis system for fast-response NO2 measurements. *J. Geophys. Res. Atmos.* 105(D21):26447-26461.
34. Crounse JD, McKinney KA, Kwan AJ, & Wennberg PO (2006) Measurement of gas-phase hydroperoxides by chemical ionization mass spectrometry. *Anal. Chem.* 78(19):6726-6732.
35. Diskin GS, Podolske JR, Sachse GW, & Slate TA (2002) Open-path airborne tunable diode laser hygrometer. *Diode Lasers and Applications in Atmospheric Sensing,* Proceedings of the Society of Photo-Optical Instrumentation Engineers (SPIE), ed Fried A), Vol 4817, pp 196-204.
36. Shetter R*, et al.* (2003) Photolysis frequency of NO2: Measurement and modeling during the International Photolysis Frequency Measurement and Modeling Intercomparison (IPMMI). *J. Geophys. Res. Atmos.* 108(D16).
37. Chan K, Dean-Day J, Bowen S, & Bui T (1998) Turbulence measurements by the DC-8 meteorological measurement system. *Geophys. Res. Lett.* 25(9):1355-1358.
38. Karion A*, et al.* (2013) Long-term greenhouse gas measurements from aircraft. *Atmos. Meas. Tech.* 6(3):511-526.
39. Mao J*, et al.* (2009) Airborne measurement of OH reactivity during INTEX-B. *Atmos. Chem. Phys.* 9(1):163-173.
40. York D (1966) LEAST-SQUARES FITTING OF A STRAIGHT LINE. *Canadian Journal of Physics* 44(5):1079-1086.

41. Gustafson WI & Yu S (2012) Generalized approach for using unbiased symmetric metrics with negative values: normalized mean bias factor and normalized mean absolute error factor. *Atmospheric Science Letters* 13:262-267.
42. Salawitch RJ*, et al.* (2002) Chemical loss of ozone during the Arctic winter of 1999/2000: An analysis based on balloon-borne observations. *J. Geophys. Res. Atmos.* 107(D20):SOL 11-11-SOL 11-20.
43. Naik V*, et al.* (2013) Impact of preindustrial to present-day changes in short-lived pollutant emissions on atmospheric composition and climate forcing. *J. Geophys. Res. Atmos.* 118(14):8086-8110.

Tables S1 to S4

Table S1. ATom observations used to derive relationships between Ω[HCHO], Ω[OH], and ΩP_{OH}. All measurements are reported at 1 Hz, except for OH and HO_2, which are reported every 30 s (ATom 1) or 20 s (ATom 2).

Measurement	**Technique**	**1σ Uncertainty**	**Reference**
HCHO	Laser-Induced Fluorescence	5% + 10 pptv	(30)
OH HO_2	Laser-Induced Fluorescence	16%	(31)
O_3 NO	Chemiluminescence	1.5% + 10 pptv 1.7% + 3 pptv	(32, 33)
H_2O_2	Chemical Ionization Mass Spectrometry	15% + 25 pptv	(34)
H_2O vapor	Open Path IR Absorption	2.5%	(35)
J(HCHO) $J(O^1D)$ $J(H_2O_2)$	Spectroradiometry + TUV v5.2[a]	15% 20% 20%	(36)
Air Pressure Air Temperature	Pitot Tube Platinum resistance thermometer	0.2 hPa 0.3 K	(37)
CO[b]	IR Cavity Ringdown Spectroscopy	9 ppbv	(38)
k'_{OH}[b]	Flow Tube	15% + 0.3 s^{-1}	(39)

[a]Tropospheric Ultraviolet and Visible radiation model, available at https://www2.acom.ucar.edu/modeling/tropospheric-ultraviolet-and-visible-tuv-radiation-model.

[b]Only used for data sub-setting in Table S2 and illustration in Fig. S2.

Table S2. Slopes of fits to subsets of column data shown in Fig. 2. Numbers in parentheses denote the number of points for each fit. Data-defined subsets (right four columns) are segregated using median value thresholds as indicated. Units for $\alpha k'_{OH}$ are s^{-1}. Uncertainties for all values are ± 0.01. Bold text indicates values that differ at the 1σ level between the two subsets.

Parameter	**Global** (139)	**Mission** ATom 1 (59) ATom 2 (80)	**Basin** Pacific (83) Atlantic (45)	**Hemisphere** South (47) North (92)	$\mathbf{f_{OH+CO}}$ [a] ≤ 0.34 (70) > 0.34 (69)	$\mathbf{\Omega NO_x}$ [b] ≤ 0.4 (70) > 0.4 (69)	$\mathbf{\Omega NO_y}$ [b] ≤ 3.1 (69) > 3.1 (70)
s_{POH} (α)	0.20	0.21	0.21	**0.24**	**0.22**	0.22	**0.23**
		0.20	0.20	**0.20**	**0.19**	0.20	**0.19**
s_{OH} ($\alpha k'_{OH}$)	0.14	0.14	0.12	0.15	0.14	0.14	**0.16**
		0.15	0.13	0.13	0.15	0.14	**0.12**

[a]Fraction of OH loss due to reaction with CO, calculated as $\Omega(k_{OH+CO}[OH][CO]) / \Omega(k'_{OH}[OH])$. For this calculation only, observed k'_{OH} is used.
[b]Subset thresholds given in units of 10^{15} cm^{-2}.

Table S3. Sensitivity of statistics for X[OH] (10^6 cm^{-3}) to various assumptions. Upper rows show results when averaging is limited to latitudes between 60°S and 60°N, where OMI data is usually valid for both missions. Lower rows show averages when X[OH] is calculated using separate slopes for the North and South Hemispheres (Table S2). All averages are weighted by tropospheric mass. Uncertainties are 1σ.

	All X[OH]	NH X[OH]	SH X[OH]	NH/SH
Latitude ±60°				
ATom 1	1.04 ± 0.23	1.32 ± 0.27	0.81 ± 0.19	1.26 ± 0.14
ATom 2	1.08 ± 0.25	0.88 ± 0.21	1.22 ± 0.28	0.54 ± 0.03
Average[a]	1.03 ± 0.24	1.09 ± 0.24	0.99 ± 0.24	0.84 ± 0.08
Hemisphere-dependent s_{OH}				
ATom 1	1.05 ± 0.25	1.36 ± 0.31	0.78 ± 0.18	1.35 ± 0.07
ATom 2	1.04 ± 0.25	0.95 ± 0.22	1.10 ± 0.27	0.64 ± 0.06
Average[a]	0.98 ± 0.25	1.11 ± 0.27	0.89 ± 0.24	0.95 ± 0.09

[a]Gridded X[OH] is averaged over both missions prior to calculating statistics (Methods). Grid cells with missing X[OH] for one mission only are filled with 0 prior to averaging.

Table S4. Methane mass fractions and partial lifetimes against remote tropospheric OH (years). Uncertainties are 1σ and include contributions from both X[OH] and the CH_4 + OH rate constant.

	M_{Ocean}/M_{Globe}	M_{Land}/M_{Globe}	M_{Poles}/M_{Globe}	τ_{CH4} global[b]	τ_{CH4} "ocean"	τ_{CH4} "land"
ATom 1	0.66	0.26	0.08	10.1 ± 1.2	10.3 ± 3.1	7.3 ± 2.8
ATom 2	0.70	0.23	0.07	11.8 ± 1.4	10.6 ± 3.3	12.1 ± 9.6
Average[a]	0.72	0.27	0.005	11.2 ± 1.3	11.4 ± 3.7	9.8 ± 5.4

[a]Gridded X[OH] is averaged over both missions prior to calculating statistics (Methods). Grid cells with missing X[OH] for one mission only are filled with 0 prior to averaging.

[b]Global value of Prather et al. (20), scaled by factors of 0.9 (ATom 1) or 1.05 (ATom 2) to adjust for seasonal variations following Nicely et al. (22).

Figures S1 to S19

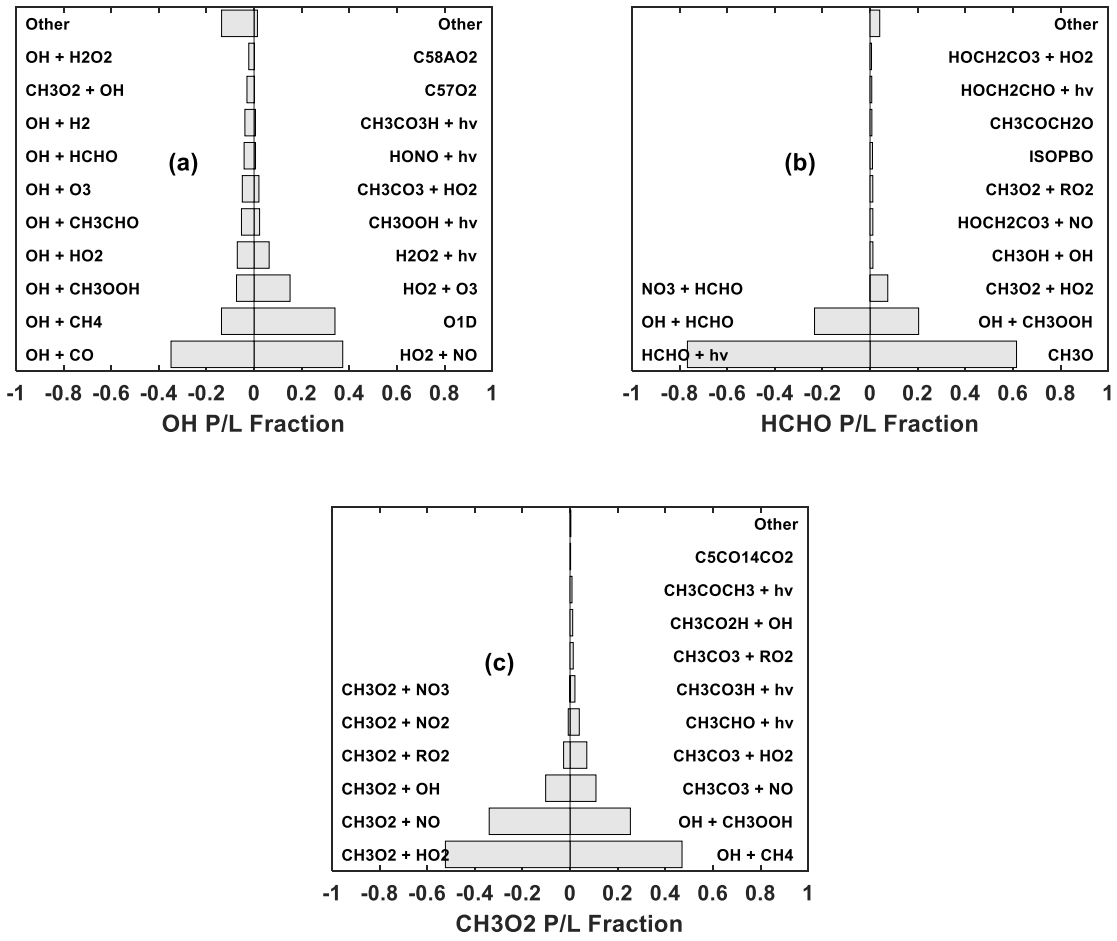

Figure S1. Average fractional production and loss rates for OH (a), HCHO (b), and CH_3O_2 (c) estimated by a measurement-constrained 0-D box model simulation. Results are averaged over all of ATom 1, excluding nighttime (SZA > 80°) and the continental US (flights 10 and 11). CH_3O_2 is the sole precursor of CH_3O, which is the primary immediate precursor of HCHO.

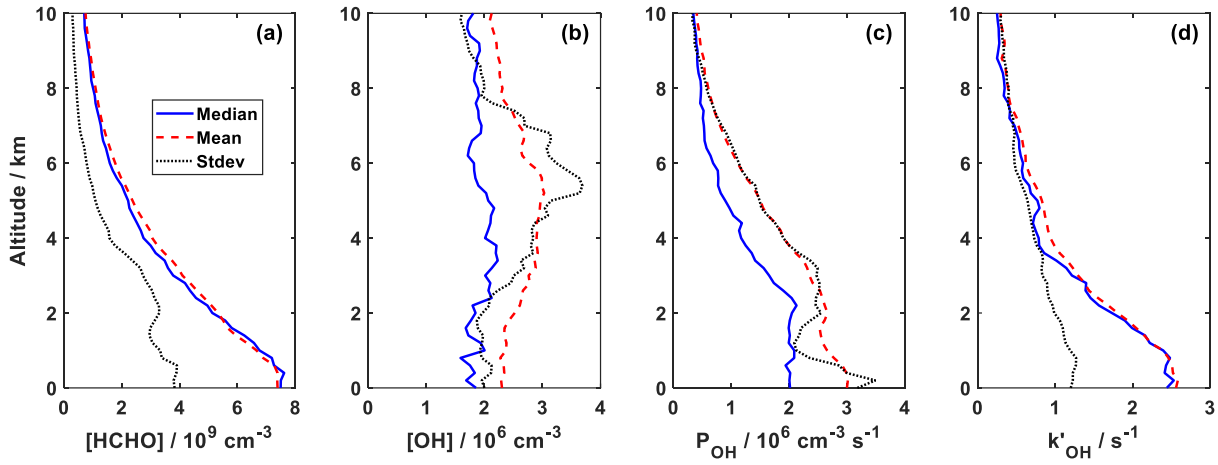

Figure S2. Statistics for ATom vertical profiles of formaldehyde (a), hydroxyl concentration (b), hydroxyl production rate (c), and total observed OH reactivity (d). Statistics (median, mean, and standard deviation) are calculated for each 200-meter bin over all valid gridded profiles (Methods).

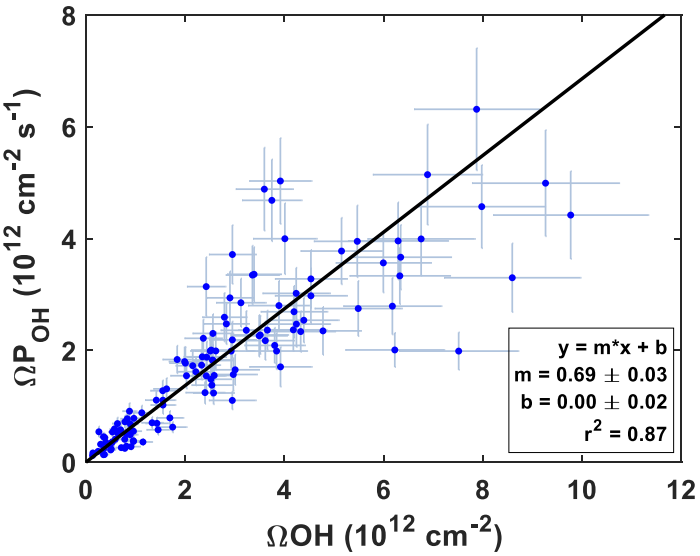

Figure S3. Correlation of total column OH concentration and production rate during ATom 1 and 2. Error bars reflect the combined 1σ uncertainty of observations and rate coefficients. The solid black line represents an uncertainty-weighted ”least-squares cubic” regression that minimizesminimize error-weighted residuals along both axes (40). Fit coefficients are given with their 1σ uncertainty. Note that ΩP_{OH} is adjusted for contributions other than those listed in (R2) – (R5) as described in Methods. The slope of this relationship is an indicator for the campaign-average column-weighted OH reactivity.

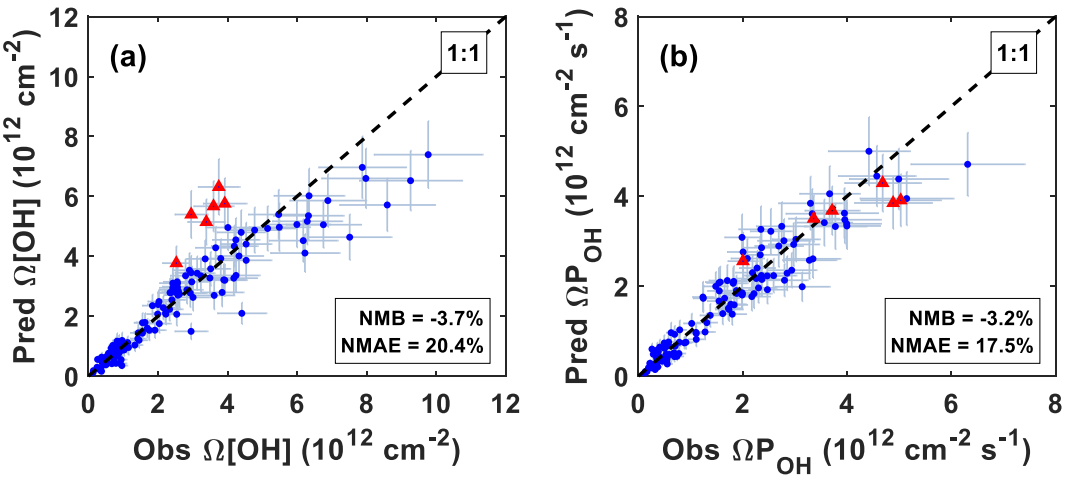

Figure S4. Comparison of ATom observed ΩP_{OH} and Ω[OH] against values predicted from ATom Ω[HCHO] by inversion of linear fits shown in Fig. 2. Error bars reflect 1σ uncertainties. Errors for predicted values include both observation and fitting contributions. Fire-impacted columns sampled near Equatorial Africa during ATom 2 are marked as red triangles. Normalized mean bias (NMB) and normalized mean absolute error (NMAE) are given following the formulation of Gustafson and Yu (41). The 1:1 line is for illustration only.

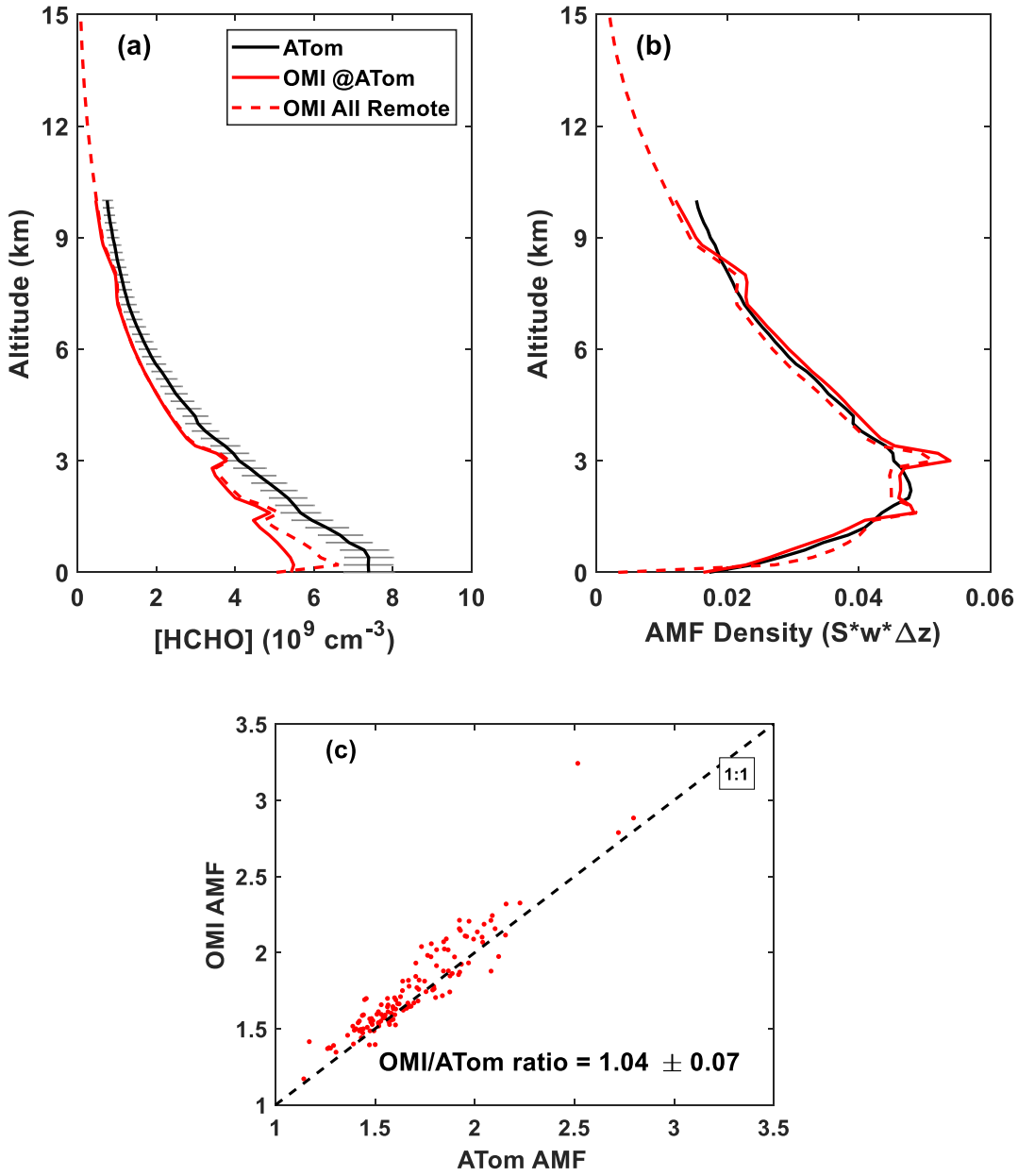

Figure S5. (a) Comparison of the mean ATom 1 and 2 HCHO vertical profile (black) with the mean OMI a priori profile for ATom profile locations only (solid red) and all remote (non-land) regions (dashed red). Thin gray lines represent the 1σ uncertainty in ATom observations. The OMI a priori extends to ~36 km. (b) Comparison of the air mass factor density, calculated by area-normalizing the profiles in (a) and multiplying the resulting "shape function" by the appropriate average scattering weight function and layer thickness. Summation of these profiles over altitude gives the AMF. (c) Comparison of the native OMI AMF with those calculated from ATom profiles as described in Text S2. The ratio of OMI to ATom AMFs (mean ± 1σ) is also shown.

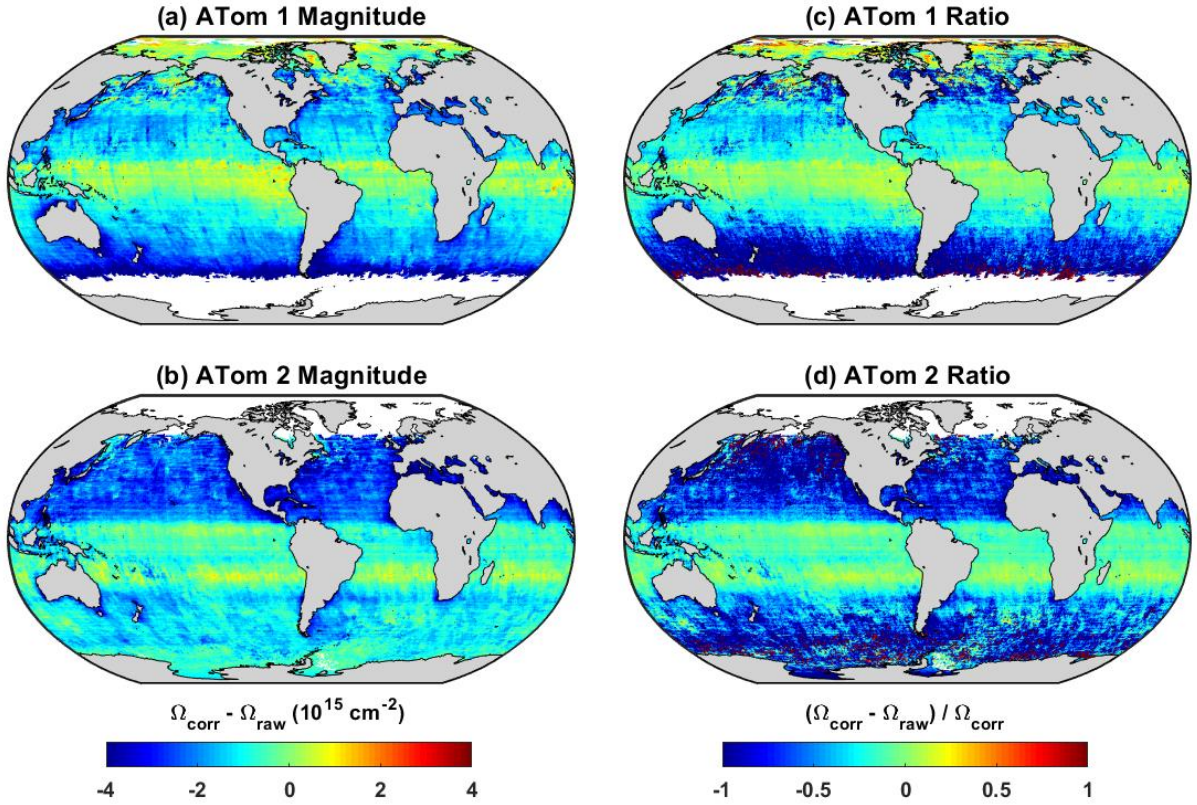

Figure S6. Absolute magnitude (a – b) and fractional contribution (c – d) of the "reference sector" correction to OMI HCHO columns for ATom 1 and 2. Ω_{raw} and Ω_{corr} respectively refer to vertical HCHO column densities before and after the correction, averaged over each mission using a precision-weighted mean. Positive values indicate regions where the correction is positive (increases Ω[HCHO]). Color bars saturate at both ends.

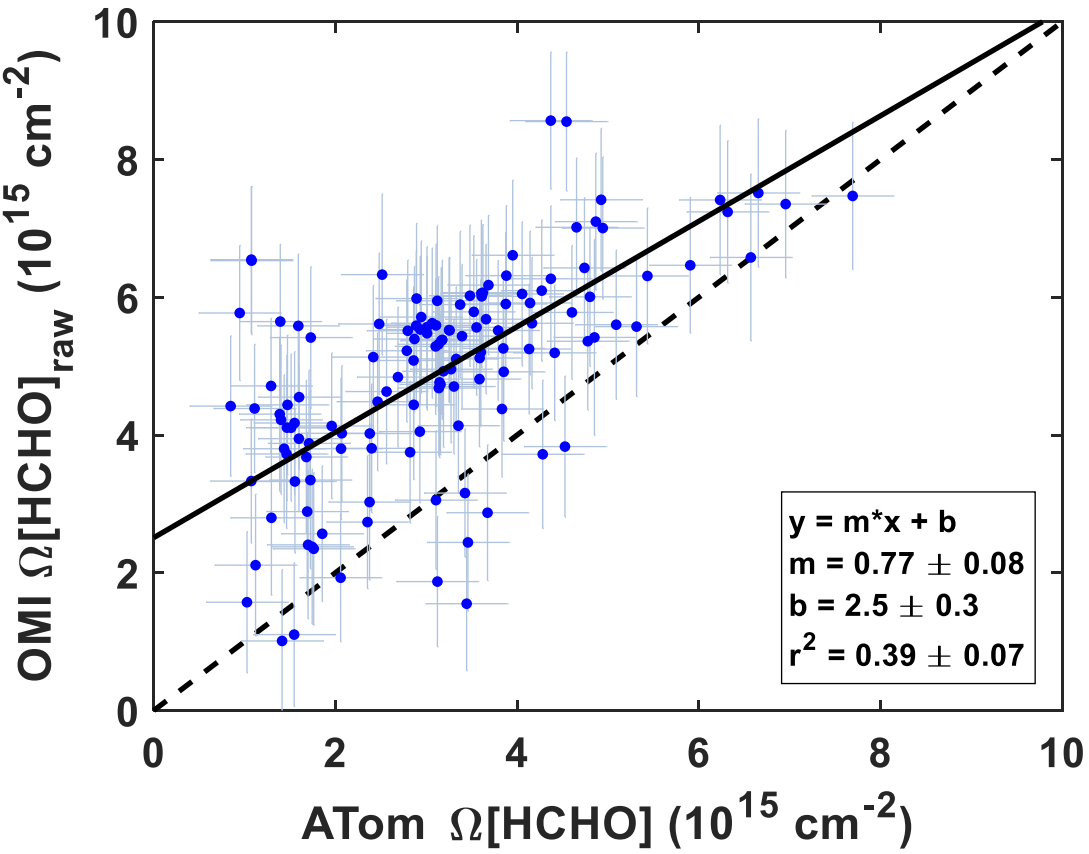

Figure S7. Comparison of the "raw" OMI SAO HCHO retrieval (prior to reference sector correction) against ATom columns. For each ATom profile, the corresponding OMI value represents an average over all grid cells intersected by the flight path. OMI columns are scaled using ATom-derived AMFs (Text S2) and corrected for the fraction of Ω[HCHO] residing below 10 km as determined by a priori profiles. The solid line is a "least-squares cubic" regression that minimizes error-weighted residuals along both axes (40). The dashed line is a 1:1 relationship. Uncertainties represent estimated 1σ precision as described in Sect. 3.2.

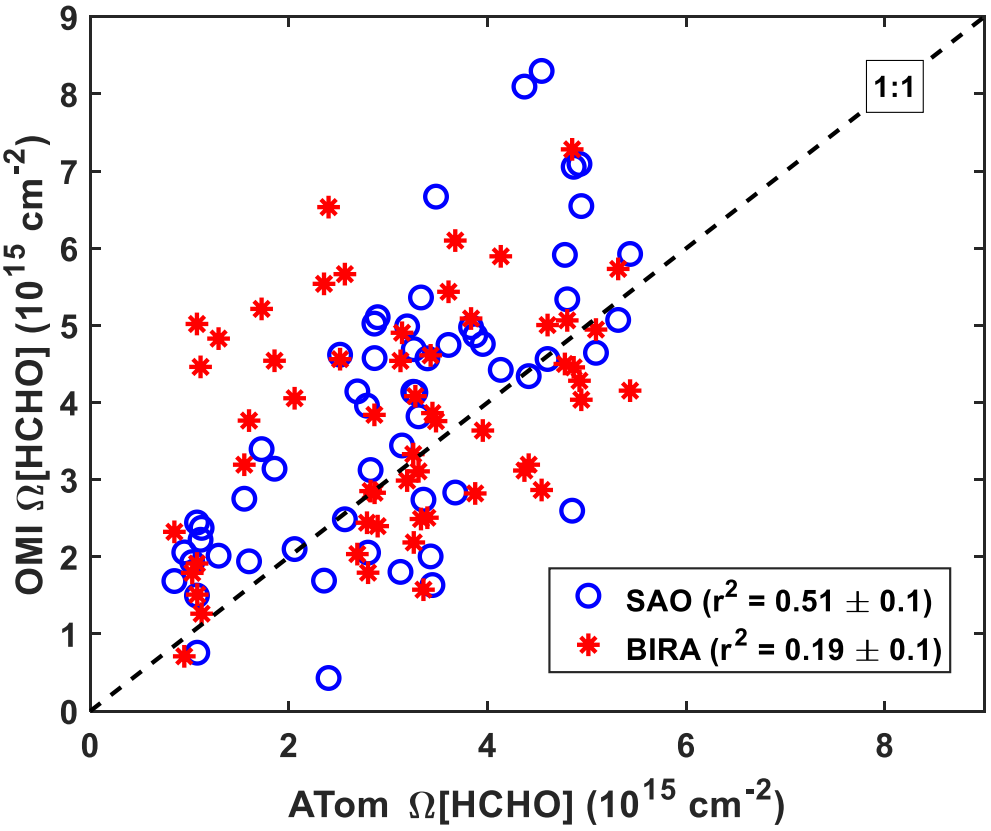

Figure S8. Comparison of two OMI retrievals against ATom 1. SAO retrievals are the same as those shown in Fig. 3 but without the minor AMF corrections. BIRA (v14) retrievals averaged over August 2016 at 0.25° x 0.25° resolution are taken from the TEMIS archive (http://h2co.aeronomie.be/) and sampled along the ATom flight track as described in Fig. 3. BIRA retrievals for ATom 2 (Feb. 2017) were not available on the TEMIS archive at the time of this analysis.

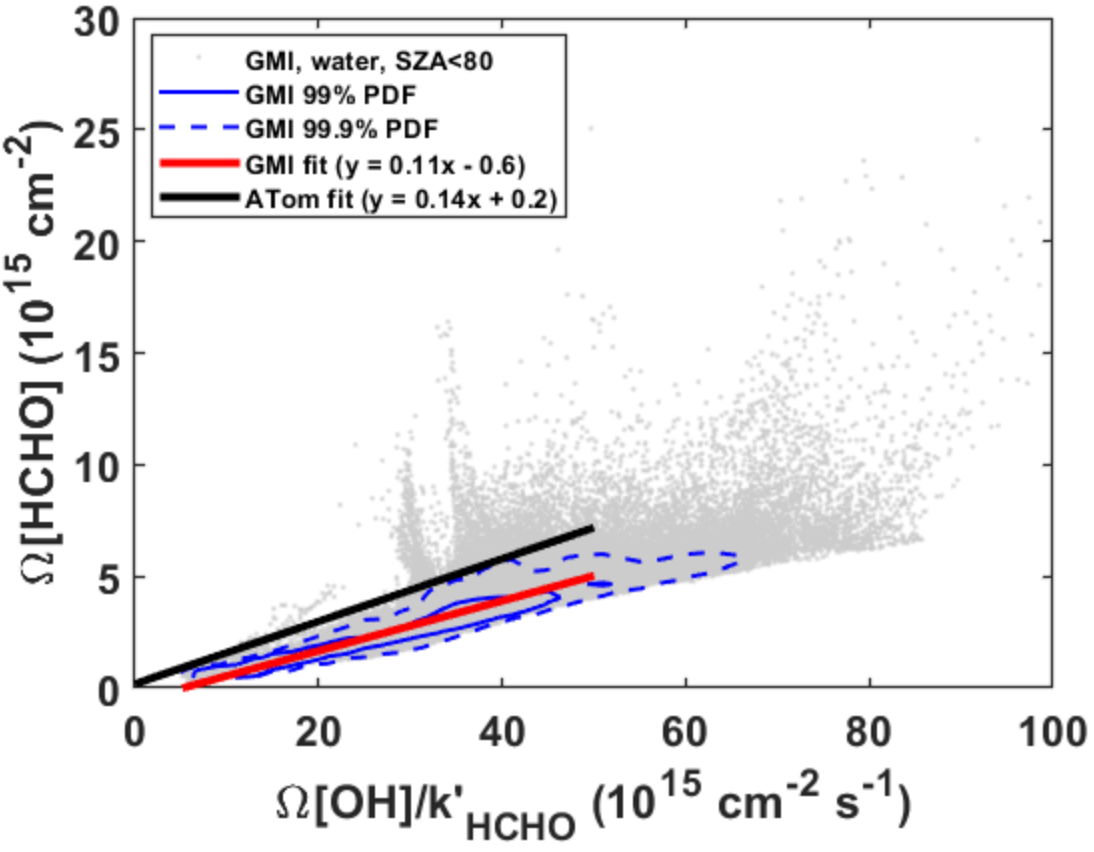

Figure S9. Relationship between column-integrated formaldehyde and OH (normalized by HCHO loss frequency) in the GMI simulation for both ATom missions. Hourly GMI output was sampled at 1300LT and averaged in each grid cell over each mission. Column mixing ratios are integrated over the pressure coordinate from the surface to the model tropopause. Gray points show individual GMI columns, filtered to only include grid cells over water and solar zenith angles below 80° (N = 245,439). Blue lines enclose model output probability at 99% (solid) and 99.9% (dash) percentiles. The red line is a reduced major axis fit of all model points falling within the range of ATom observations ($\Omega[OH]/k'_{HCHO} < 50 \times 10^{15}$ cm^{-2} s^{-1} and $\Omega[HCHO] < 8 \times 10^{15}$ cm^{-2}). The black line is the ATom fit as shown in Fig. 2(a).

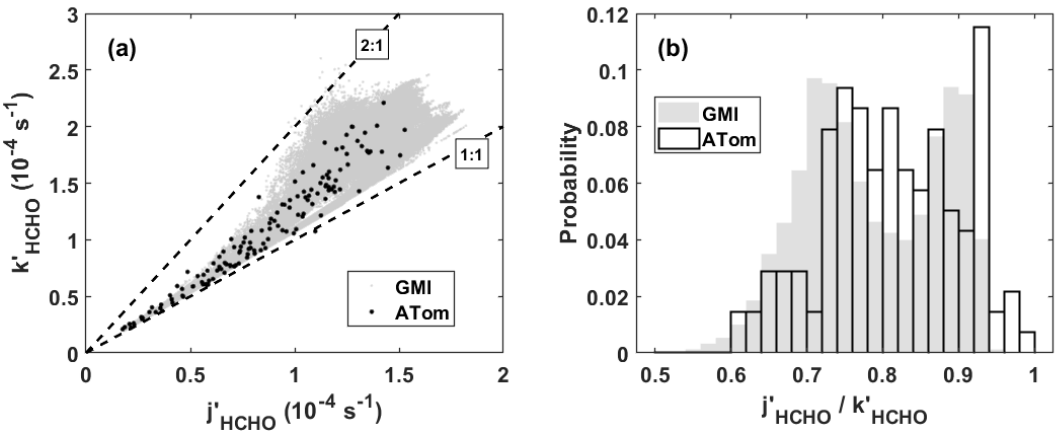

Figure S10. Comparison of GMI and ATom column-average HCHO loss frequencies for photolysis (j'_{HCHO}) and photolysis plus OH loss (k'_{HCHO}). (a) Scatter plot of all values for ATom 1 and 2. Gray points show individual GMI columns, filtered to only include grid cells over water and solar zenith angles below 80° (N = 245,439). Black points are ATom observations from all valid columns. Dashed lines show the range of slopes. (b) Distribution of the fraction of photolysis contributing to total HCHO loss in the column.

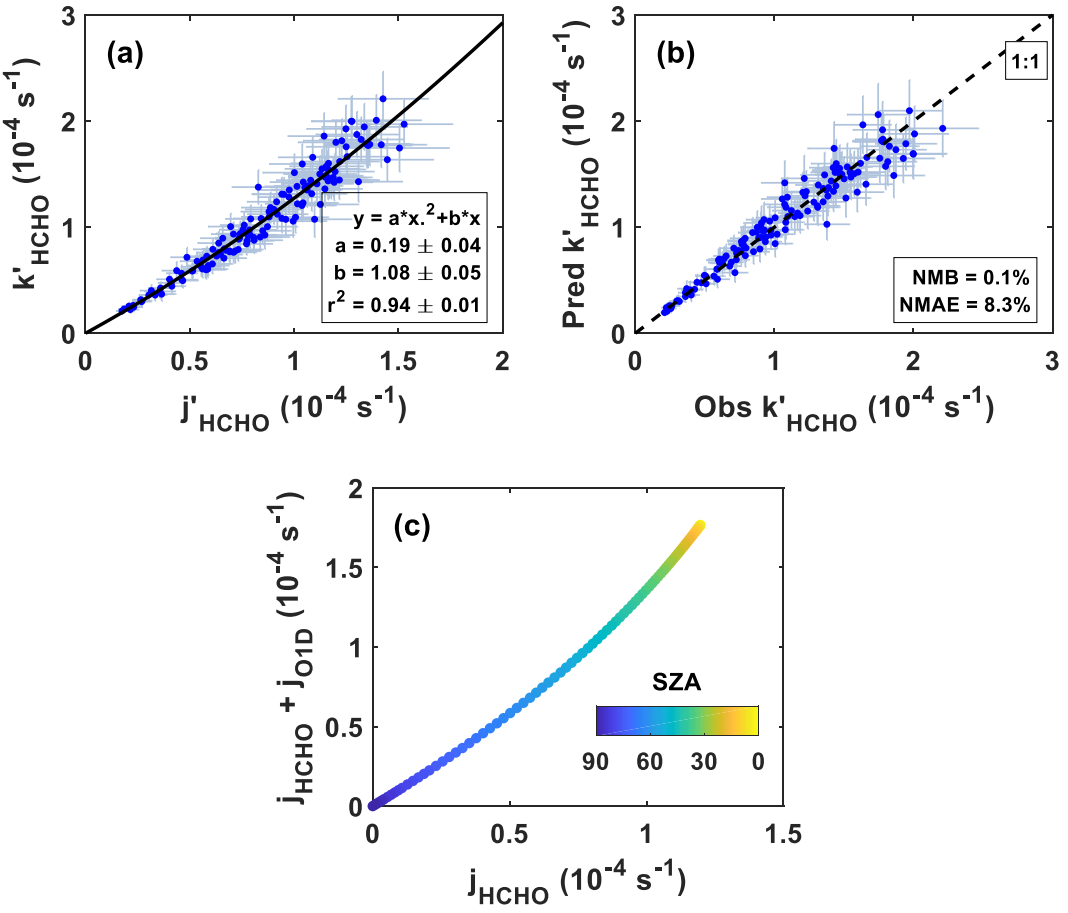

Figure S11. (a) Correlation of ATom column-weighted HCHO loss frequencies for photolysis-only and total loss (photolysis plus OH reaction). Error bars reflect the combined 1σ uncertainty of observations and rate constants. The solid black line represents an unweighted ordinary least-squares quadratic regression with the intercept forced to zero; fit coefficients are given with their 1σ uncertainty. (b) Comparison of observed k'_{HCHO} with values predicted from j'_{HCHO} and the relationship shown in (a). NMB and NMAE are as described in Fig. S4. (c) Example theoretical quadratic relationship between HCHO photolysis and its sum with $O(^1D)$ production from O_3 photolysis (the latter being a loose marker for photolytic OH production). J-values are calculated from the Tropospheric Ultraviolet and Visible Radiation Model (TUV v5.2) as implemented in F0AM (23) using nominal inputs of altitude = 1 km, overhead O_3 column = 300 DU, and surface albedo = 0.06. Curvature as the sun nears zenith is due to the increased flux of UV radiation, which preferentially enhances O_3 photolysis.

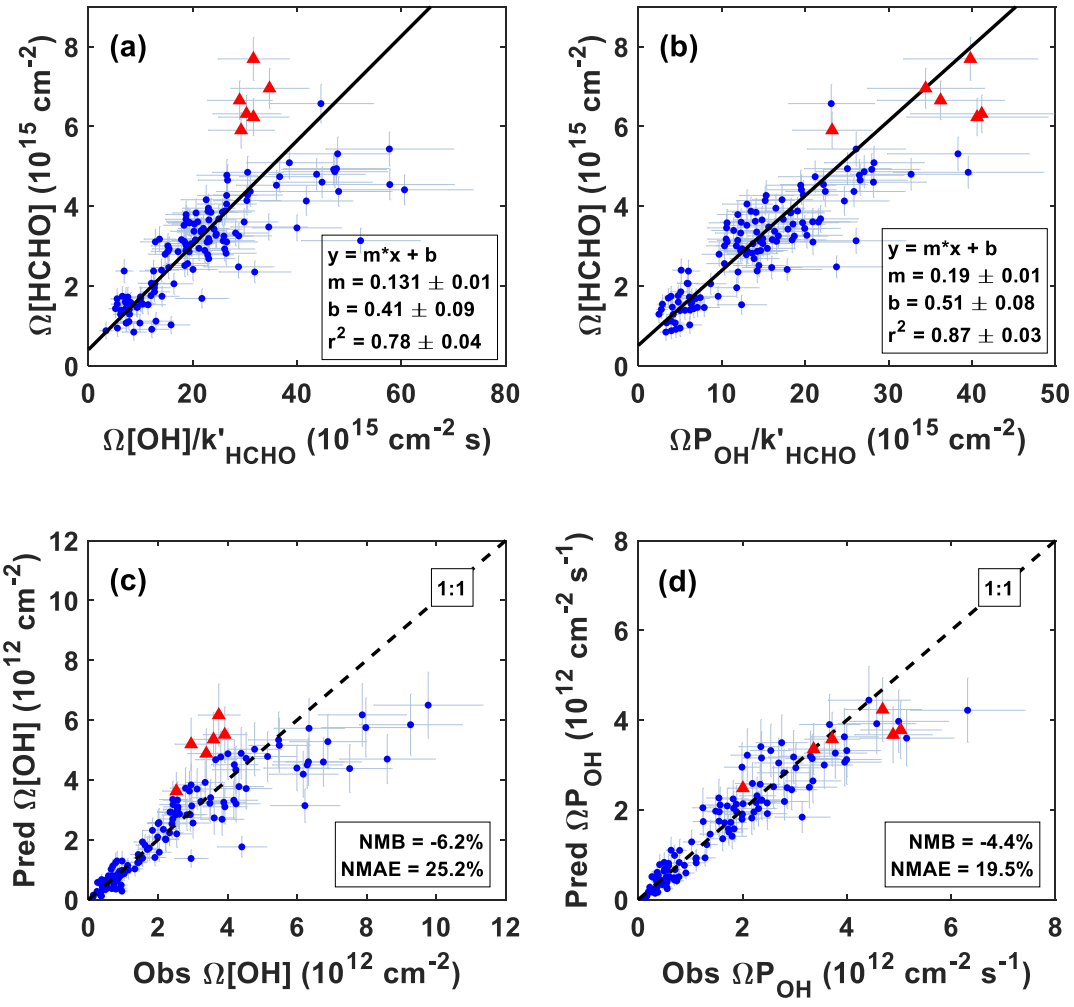

Figure S12. As in Figs. 2 and S4, but using k'$_{HCHO}$ predicted from j'$_{HCHO}$ via the ATom scaling coefficients (see previous figure).

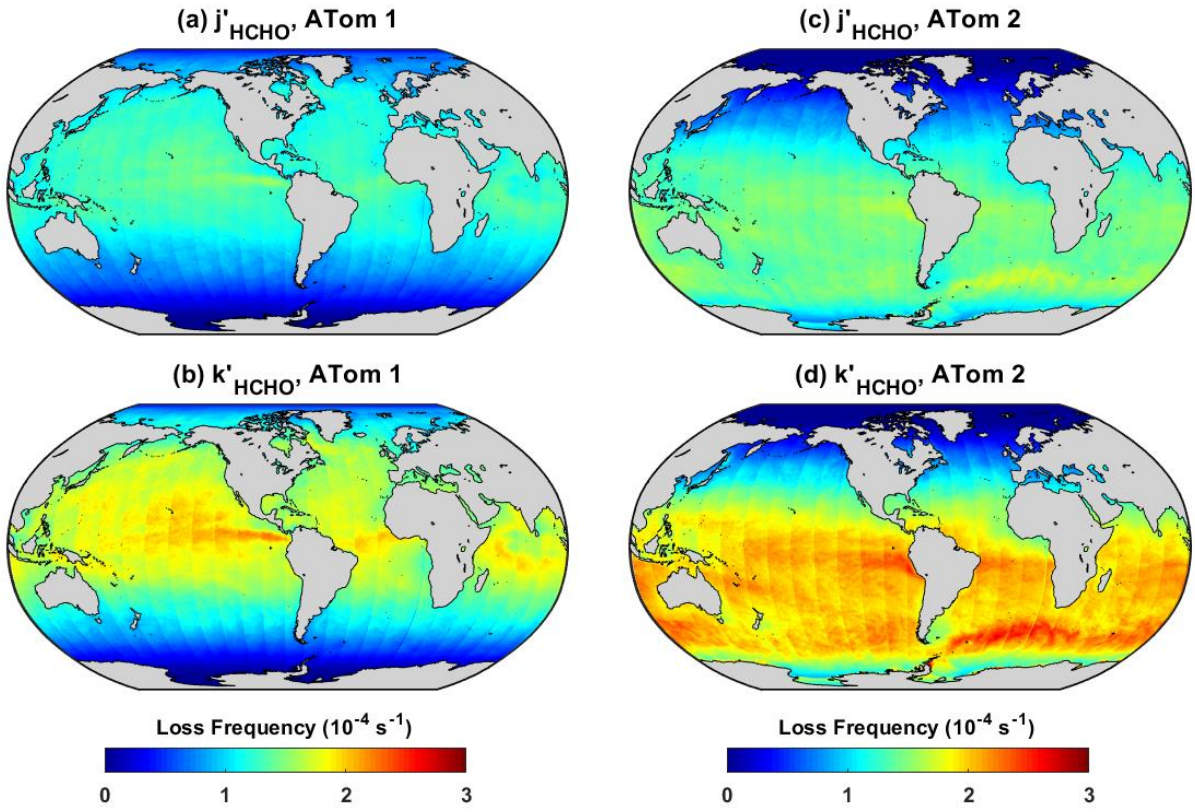

Figure S13. Column-weighted HCHO photolysis frequencies (a and c) and total loss frequencies (b and d) derived from the GMI simulation for ATom 1 and 2. Values for j'_{HCHO} are from GMI model output sampled at 1300 LT and averaged over the mission period. Column integration is from the surface to the model tropopause. k'_{HCHO} is calculated from j'_{HCHO} using the ATom relationship shown in Fig. S11a. Vertical banding is due to the use of hourly output for 1300 LT, which changes at intervals of 15 degrees longitude.

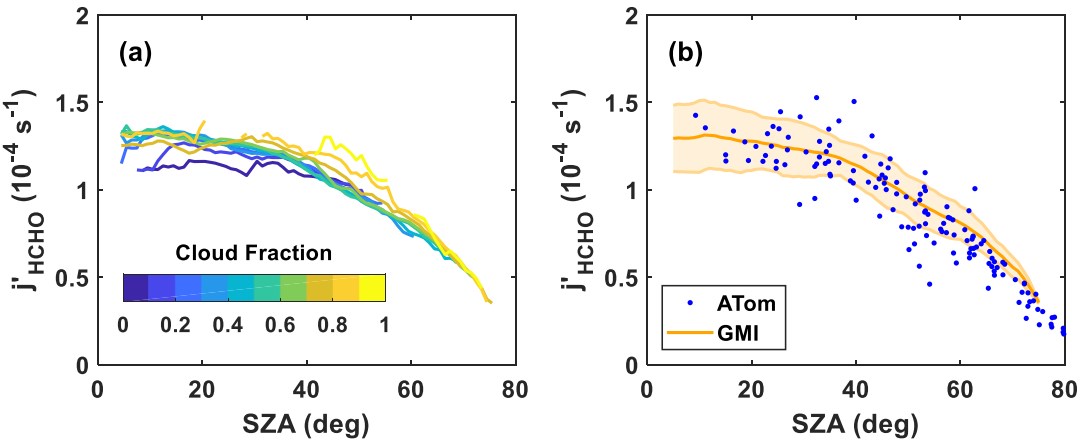

Figure S14. Evaluation of GMI column-weighted HCHO photolysis frequencies. Model values were extracted from hourly output at 1300 LT for open water grid cells corresponding to valid OMI observations and temporally averaged over the ATom 1 period. (a) Dependence of j'_{HCHO} on average cloud fraction. Model values are binned by cloud fraction and solar zenith angle in increments of 0.1 and 2°, respectively. (b) Agreement of model j'_{HCHO} with ATom 1 and 2 observations. The orange shaded region signifies the 2σ variability about mean model values.

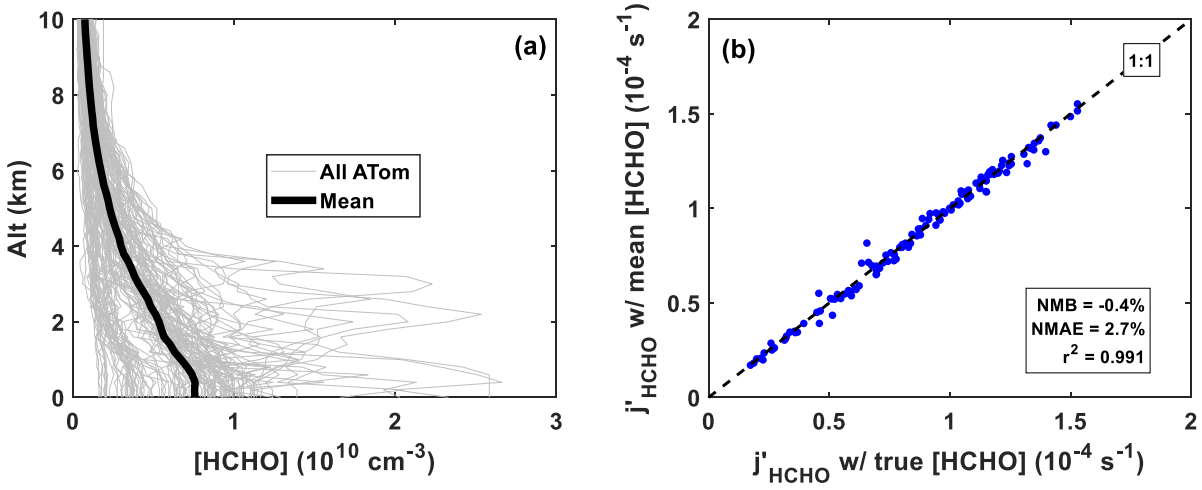

Figure S15. Evaluation of [HCHO] vertical profile effects on column-weighted photolysis frequencies. (a) All [HCHO] vertical profiles for ATom 1 and 2 (gray lines), gridded and filtered as described in Methods. The thick black line is the mean profile. (b) Comparison of j'_{HCHO} for all ATom profiles calculated with the observed ("true") or mission-mean [HCHO] profiles. NMB and NMAE are as defined in Fig. S3.

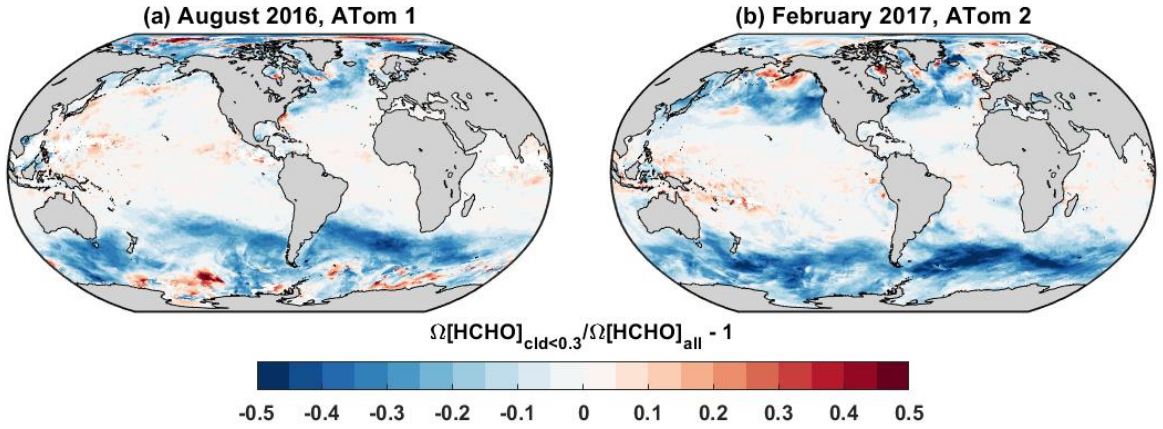

Figure S16. Effects of cloud-filtering on GMI Ω[HCHO]. Hourly model output is averaged over each mission either with or without a filter to exclude columns with cloud fractions > 0.3. Colors indicate the relative bias of the cloud-filtered or "clear sky" average relative to the unfiltered or "all sky" average for ATom 1 (left) and 2 (right).

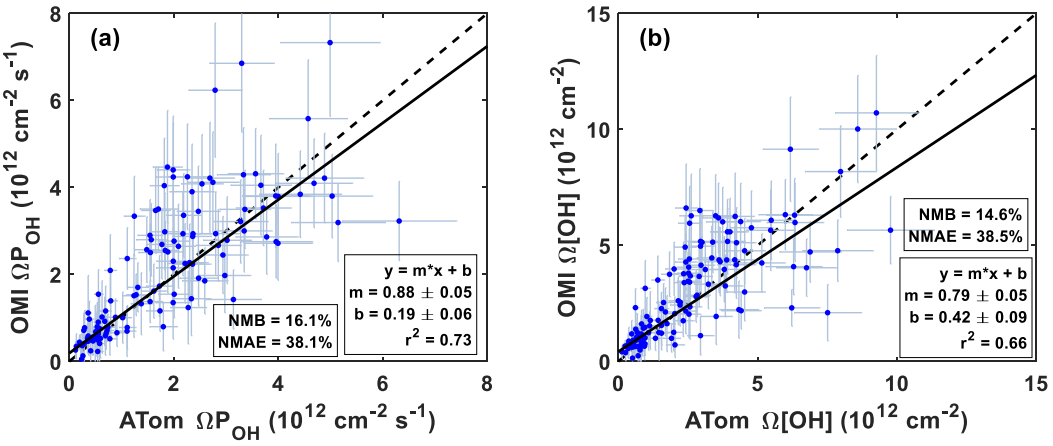

Figure S17. Comparison of OMI-inferred tropospheric column OH production rates (a) and concentrations (b) to ATom observations. OMI-inferred values are extracted from the campaign-average datasets shown in Fig. 4. For each ATom profile, the corresponding OMI-inferred value represents the average over all grid cells intersected by the flight path. OMI-inferred columns are corrected for ATom-derived AMFs (Text S1) and for the fraction of Ω[HCHO] residing below 10 km as determined by a priori profiles. They are also scaled by a factor of $\cos(SZA_{ATom})/\cos(SZA_{OMI})$ to correct for differences in the time of observation. The solid line is an uncertainty-weighted ordinary least squares regression. The dashed line is a 1:1 relationship shown for comparison. All uncertainties are 1σ. NMB and NMAE are as described in Fig. S4.

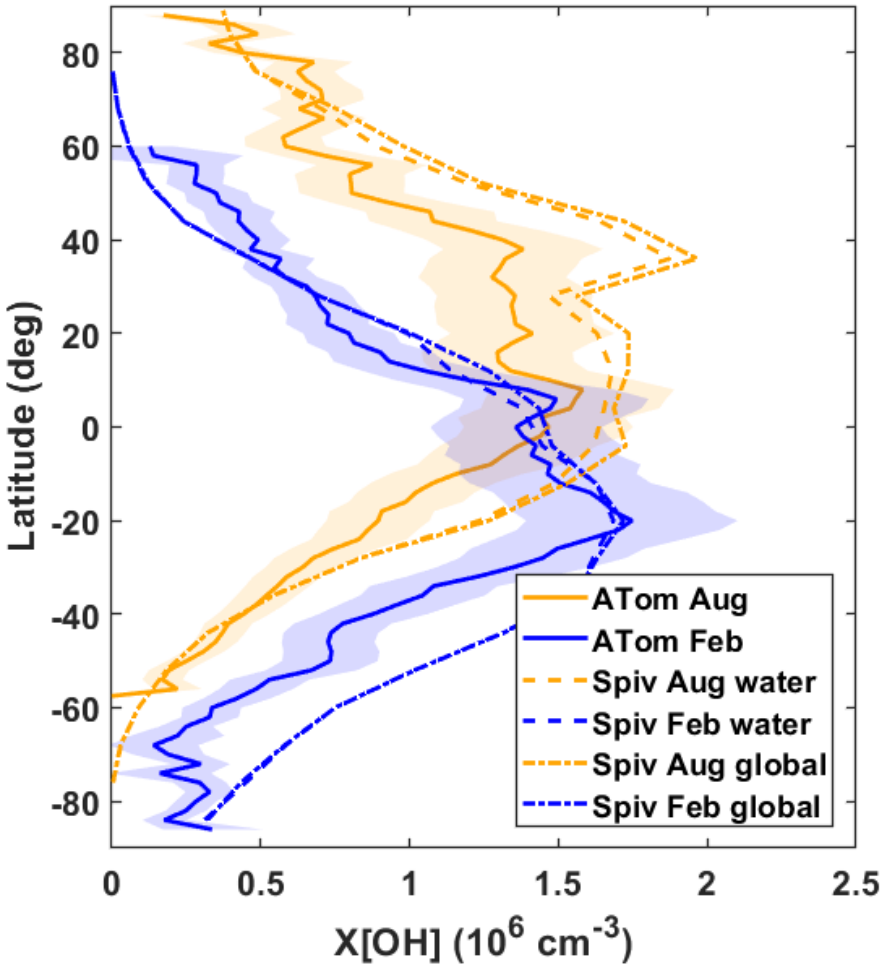

Figure S18. Comparison of zonal mean X[OH] against the box model climatology of Spivakovsky*, et al.* (19). ATom results are as described in Fig. 5. Spivakovsky monthly 3-D fields are converted to column-mean [OH] by integration over the pressure coordinate (42) and normalization by maximum altitude (100 hPa for latitudes within ±32°, 200 hPa otherwise). Dotted lines are zonal averages over the whole globe and dashed lines are averages for grid cells with more than 50% of the surface defined as water.

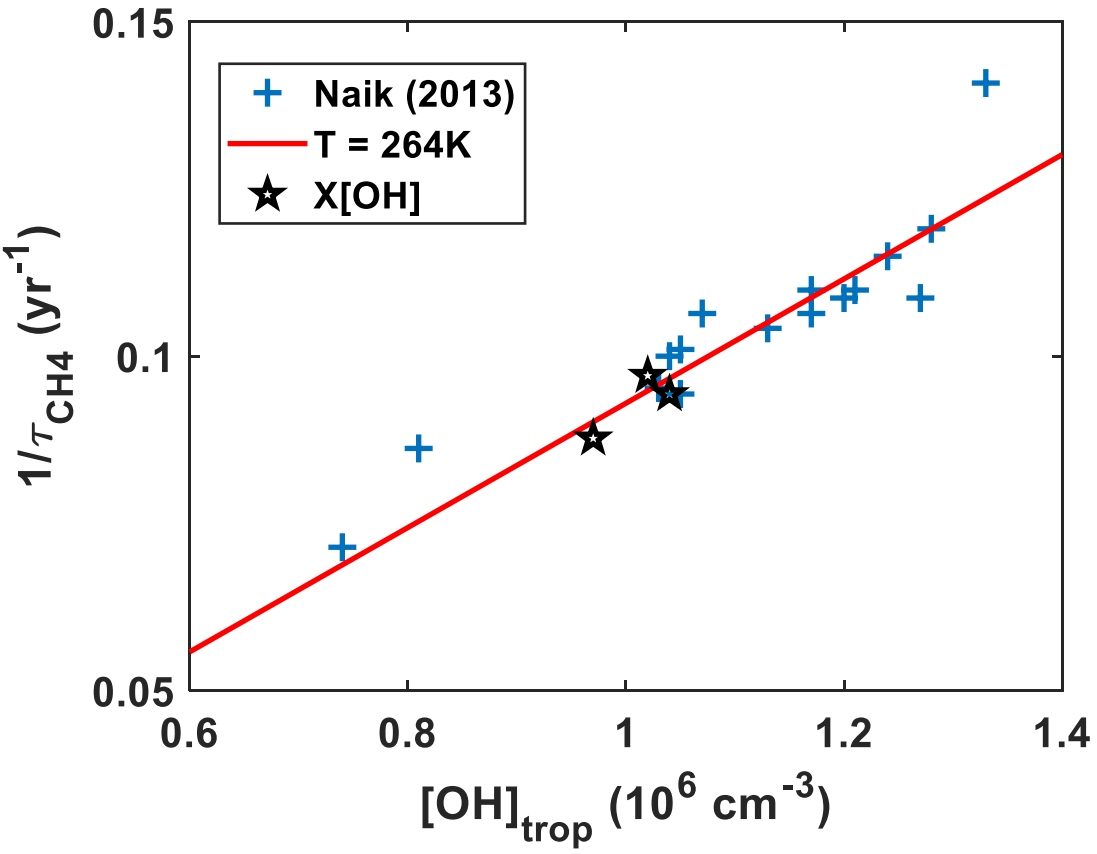

Figure S19. Global tropospheric mean [OH] and total CH_4 loss frequency due to OH are highly correlated. Blue crosses show all individual global model estimates from the year 2000 columns of Table 1 of Naik, *et al.* (43). Based on the simple formulation of $(\tau_{CH4})^{-1} = k(T_{eff})[OH]_{trop}$ and a rate coefficient of k = 2.45E-12 exp(-1775/T) (12), the model relationship is best fit by an effective air temperature of T_{eff} = 264K (red line). Black stars indicate X[OH]-based estimates from each ATom mission and the average of both missions. The latter includes zero-filling for grid cells missing data from one mission or the other, thus the average is lower than the value from each mission.